IEEE Photonics Journal
An IEEE Photonics Society Publication

Open Access

Femtosecond Laser Direct Ablating Micro/Nanostructures and Micropatterns on $CH_3NH_3PbI_3$ Single Crystal

Volume 9, Number 2, April 2017

Chao-Wei Wang
Yang-Yang Dang
Ya-Hui Su
Jin-Cheng Ni
Chen-Chu Zhang
Jia-Wen Li
Yan-Lei Hu
Jia-Ru Chu
Wen-Hao Huang
Dong Wu
Xu-Tang Tao

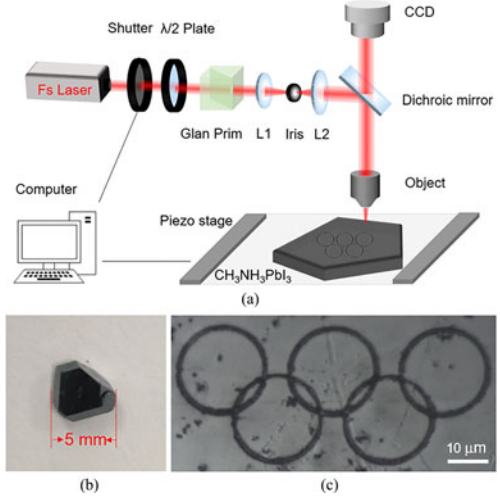

DOI: 10.1109/JPHOT.2017.2676353
1943-0655

Femtosecond Laser Direct Ablating Micro/Nanostructures and Micropatterns on $CH_3NH_3PbI_3$ Single Crystal

Chao-Wei Wang,[1] Yang-Yang Dang,[2] Ya-Hui Su,[3] Jin-Cheng Ni,[1] Chen-Chu Zhang,[1] Jia-Wen Li,[1] Yan-Lei Hu,[1] Jia-Ru Chu,[1] Wen-Hao Huang,[1] Dong Wu,[1] and Xu-Tang Tao[2]

[1]CAS Key Laboratory of Mechanical Behavior and Design of Materials, Department of Precision Machinery and Precision Instrumentation, University of Science and Technology of China, Hefei 230026, China
[2]State Key Laboratory of Crystal Materials, Shandong University, Jinan 250100, China
[3]School of Electrical Engineering and Automation, Anhui University, Hefei 230601, China

DOI:10.1109/JPHOT.2017.2676353

Manuscript received January 18, 2017; revised February 21, 2017; accepted February 23, 2017. Date of publication March 8, 2017; date of current version March 17, 2017. This work was supported in part by the National Science Foundation of China under Grant 51275502, Grant 61475149, Grant 51405464, Grant 61675190, Grant 51321091, and Grant 51675503; in part by the Fundamental Research Funds for the Central Universities (WK6030000004 and WK2480000002); and in part by the Chinese Thousand Young Talents Program. Corresponding authors: D. Wu and X.-T. Tao (e-mail: dongwu@ustc.edu.cn; txt@sdu.edu.cn).

Abstract: Single crystal perovskite materials with the intriguing properties of wide optical absorption range, low trap density, photoluminescence, and superior charge-transfer have emerged as a new class of revolutionary photovoltaic semiconductors promising for various applications. A technique to realize microstructures or microdevices on the surface of single crystal can facilitate the incorporation of these materials into optoelectronic applications. Here, we first reported the fabrication of 1-D mciropores, microlines, and 2-D micropatterns such as word "USTC," number "2016" and "Olympic rings" on the surface of $CH_3NH_3PbI_3$ single crystal by femtosecond laser ablating. The effect of parameters such as exposure time, laser peak intensity, and scanning speed was quantitatively investigated to determine the parameter intervals capable of ensuring the required resolution. By fabricating periodic grating microstructures, the perovskite surfaces showed bright iridescence from dark blue to red due to the grating diffraction effect. Moreover, it is found that the fluorescence peak strength of processed area obviously grows with laser peak intensity and scanning speed, which is attributed to the increasing surface roughness caused by higher laser peak intensity and slower scanning speed. These works are beneficial for researchers to better understand the intrinsic property of single crystal perovskite and accelerate perovskite-based optoelectronics applications.

Index Terms: Femtosecond laser microfabrication, single crystal perovskite, controllable microstructures and micropatterns, fluorescence enhancement.

1. Introduction

As we all know, the switch of energy structure and the discovery of the green power for sustainable development have become a heated topic for many countries confronted with severe energy situation and the deterioration of eco-environment. Methyl-ammonium lead halide materials with a perovskite crystal structure ($MAPbX_3$, where X = Cl, Br, or I), as a new class of solar absorber

materials, have recently demonstrated excellent performances in optoelectronic fields [1]–[5]. Since the discovery that halide perovskite materials can be used as solar absorbers, the power conversion efficiency (PCE) of perovskite solar cells has been increased from 3.8% [6] to 22.1% [7] in the past six years. The high performance of halide perovskite solar cells has been attributed to their low non-radiative recombination, wide optical absorption range, high carrier mobility and low trap density [8]. However, most of present reports [9]–[11] are based on microcrystalline and thin polycrystalline films for perovskite solar cells and other optoelectronic devices, which still faces significant challenges. For example, serious efficiency losses caused by recombination of carriers would happen due to lots of grains, boundaries, voids, and surface defects in perovskite material. Compared with microcrystalline and thin polycrystalline films, organic-inorganic hybrid perovskite single crystal [12], [13] shows better thermal stability, wider absorption range and higher carrier mobility, and thus optoelectronics devices would have better photoelectric properties [14]–[16]. In the future, single crystal material could be processed for micro/nanodevices and miniaturized integrated microsystems. However, perovskite is highly sensitive to damp and fragile, making it susceptible to material degradation, decomposition and broken in solution-based or contact mode fabrication processing, which hinders the micro/nanofabrication on its surface or interior. For example, fabrication of micro/nanodevices using photo- or electron beam-lithography techniques causes decomposition of the perovskite during the photoresist baking, solvent development process or thermal evaporation. Similarity, lithographie, galvanoformung, and abformung (LIGA) or nanoimprint lithography techniques causes fragmentation during the pressing molding. Therefore, these methods are not suitable for the microfabrication of single-crystal perovskite. Alternatively, femtosecond laser micro-nanofabrication technology [17]–[23] provides the capability of direct maskless patterning on most materials for device prototyping. This technology has many unique advantages such as high resolution, non-solution-based approach, maskless 3-D processing ability, negligible thermal-diffusion effect, and wide applicability of materials. Thus, femtosecond laser fabrication on perovskite is straightforward without requirement of subsequent development or etch-back or lift-off device processing, which is required in the lithographic routine.

In this paper, we firstly reported the fabrication of various microstructures and two-dimensional micropatterns on the surface of $CH_3NH_3PbI_3$ perovskite single crystal by femtosecond laser ablating. Then, the effect of laser processing parameters was quantitatively investigated in order to determine the parameter intervals capable of ensuring the required resolution. Moreover, colorful perovskite surfaces were obtained by fabricating periodic grating microstructures. In the end, the fluorescence properties of laser processed materials were systematically studied and characterized. The obvious fluorescence intensity enhancement shows a promising application of this technique in perovskite surface emission LEDs. Highly uniform nanopatterning and surface roughening by utilizing femtosecond laser ablating could provide a direct approach for achieving nanostructures or improving the performance of perovskite-based optoelectronic devices.

2. Perovskite Crystal Growth and Microstructure Processing by Femtosecond Laser Ablation

Here, the bottom seeded solution growth (BSSG) method [24] is used for the crystal growth of the $CH_3NH_3PbI_3$ perovskite material where the crystal growths are both easily controlled and maintained stable. The solubility of the organ-halide perovskites in the corresponding acid halide solvents is moderate at room temperature but changes considerably with temperature. By dipping the preferred seed into the solvent and lowing the temperature accurately, the crystal growth will take place on the seed and high quality large single crystals [see Fig. 1(b)] can be obtained finally. The decrease in the solution temperature induces saturation of the solute, and the saturated aqueous perovskite precursor HI solution containing an inorganic metal salt and an organic halide salt forms halide perovskite crystals slowly.

The halide perovskite structure has a general ABX_3 (X = F, Cl, Br, or I) formula, where A and B cations coordinate with 12 and 6 X anions, forming cuboctahedral and octahedral geometry,

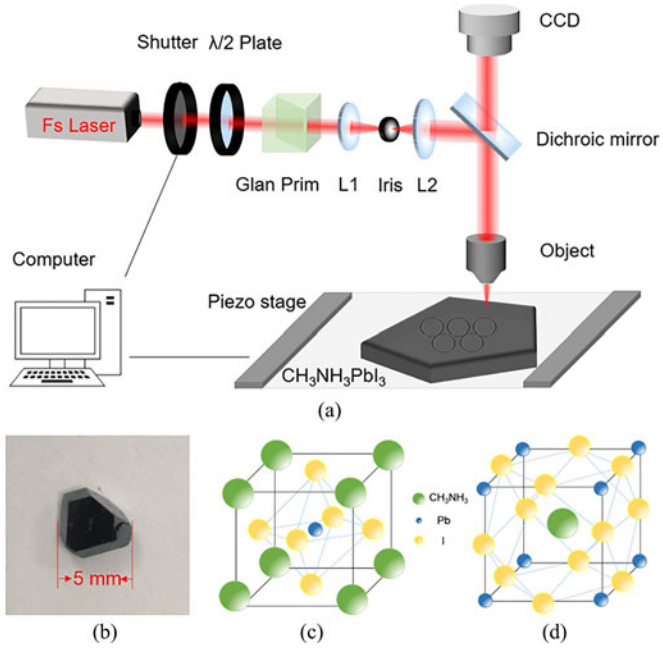

Fig. 1. Schematic diagram of femtosecond laser ablating system and photograph taken from the as-grown crystal. (a) Schematic diagram of femtosecond laser ablating system. The power of femtosecond laser was modulated with a half wave plate and a Glan Laser beamspliter. (b) Optical photograph of $CH_3NH_3PbI_3$ single crystal. The dimension is 5 mm $\times$ 3.5 mm $\times$ 2 mm. ABX_3 perovskite structure shows (c) BX_6 octahedral and (d) AX_{12} cuboctahedral geometry.

respectively. A and B are the representative of cations for different sizes, and the A cation is larger than the B cation. The crystal structure is shown in Fig. 1(c) and (d). Perovskite formation can be estimated simply by using the Goldschmidt tolerance factor (t) and the octahedral factor (μ), t and μ are defined as following formula [25]:

$$t = (R_A + R_X)/2^{1/2}(R_B + R_X)] \quad (1)$$

$$\mu = R_B/R_X \quad (2)$$

where R_A, R_B, and R_X are the effective ionic radii for the ions in the A, B, and X sites, respectively.

In general, for halide lead perovskite, $0.81 < t < 1.11$ and $0.44 < \mu < 0.90$. If t is in a small range (0.89–1.0), perovskite structure is a cubic. When t is lower than the range mentioned above, the perovskite structure may exhibit asymmetric tetragonal or orthorhombic. Even through different structures may be formed in different conditions, all kinds of perovskite structures will change by heating. After high temperature treatment, these irregular structure usually convert to cubic crystal structure [25].

Fabricating microstructures/devices are important for their optoelectronic application, however it is always challenging due to its fragility and easy decomposition under humid environment. Here, we proposed a new strategy of femtosecond laser ablating which has many unique advantages such as non-solution-based approach, maskless 3-D processing ability, and negligible thermal-diffusion effect to directly fabricate arbitrary microstructures on perovskite Surface. The experimental setup of femtosecond laser ablating system is shown in Fig. 1(a). The laser source is a mode-locked Ti:sapphire ultrafast oscillator (Coherent, Chamleon Vision-S) with central wavelength at 800 nm, pulse duration of 75 fs, and repetition rate at 80 MHz. After passing through a shutter, the power of femtosecond laser was modulated with a half wave plate and a Glan Laser beam spliter. Subsequently, the laser pass through an inverse telescope and focused by a microscope object (50$\times$, N.A. $=$ 0.8) on perovskite surface. The inverse telescope system contain two lenses and an Iris

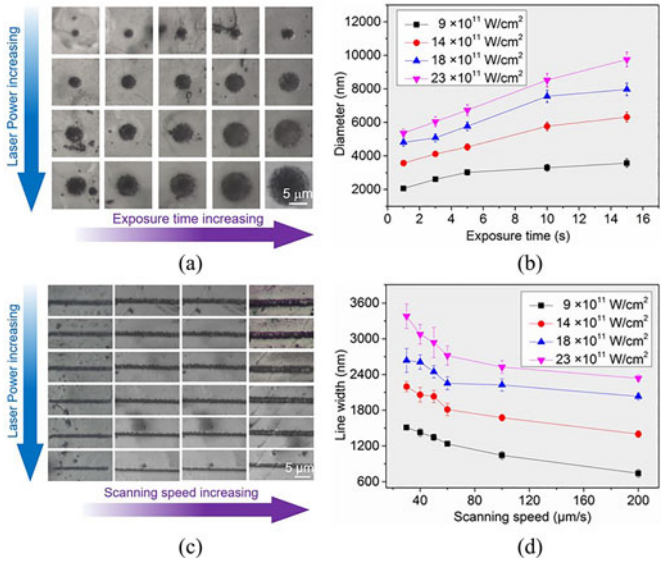

Fig. 2. Relationship between laser processing parameters and dot diameter, as well as line width. (a) Optical microscope images of dots for exposure time ranging from 1 s to 15 s and laser peak intensity ranging from 9×10^{11} W/cm^2 to 2.3×10^{12} W/cm^2. (b) Relationship between exposure time and diameter of dot. The maximum dot diameter is 9.8 μm, and the minimum is 2.1 μm. (c) Optical microscope images of lines with scanning speed ranging from 30 μm/s to 200 μm/s and laser peak intensity ranging from 9×10^{11} W/cm^2 to 2.3×10^{12} W/cm^2. (d) Relationship between scanning speed and line width. The maximum and the minimum of line width are 3.4 μm and 0.7 μm, respectively.

which positioning at the focal plane of the L1. The size of the focused laser spot on the sample is about 1.2 μm. The sample is mounted on a nano-positioning stage (Physik Instrument, E545) with a resolution of 0.1 nm and a 200 μm $\times$ 200 μm $\times$ 200 μm moving range. The processing can be observed by the Charge Coupled Device (CCD) in real time. By precisely controlling the nano-positioning stages, two-dimensional microstructures and micropatterns would be fabricated on the $CH_3NH_3PbI_3$ single crystal surface [see Fig. 1(b)]. Since the processed area is much smaller (1-1500 μm), the microscopic and SEM images shown in the following figures were the magnified microstructures. All the experiments are carried out under ordinary room temperature conditions in air.

3. The Relationship Between Laser Processing Parameters and Dot Diameter and Line Width

In the experiment of femtosecond laser ablating on perovskite surface, the laser induced microstructures are systemically studied by varying parameters including laser peak intensity, exposure time and scanning speed. In our previous works [24], we reported the black and shiny crystal $CH_3NH_3PbI_3$ was not hygroscopic and had relatively good stability after being exposed to air for several days at room temperature. Especially in clean room, the low humidity ($<$30%) can keep the perovskite crystal stable during the process of femtosecond laser ablating, which only costs several hours ($<$3 h). First, the effect of exposure time ranging from 1 s to 15 s and laser peak intensity ranging from 9×10^{11} W/cm^2 to 2.3×10^{12} W/cm^2 on single dot processing were studied [the optical microscopy images in Fig. 2(a) and SEM image in Fig. 3(a)], which shows that dot diameter becomes bigger with the increase of exposure time or the laser peak intensity. When the laser peak intensity is fixed at 9×10^{11} W/cm^2 and 1.4×10^{12} W/cm^2, uniform dots are achieved and the dot diameter can be precisely controlled in a range from 2 μm to 6.3 μm by modulating the exposure time from 1 s to 15 s. When the laser peak intensity is increased to 1.8×10^{12} W/cm^2 and

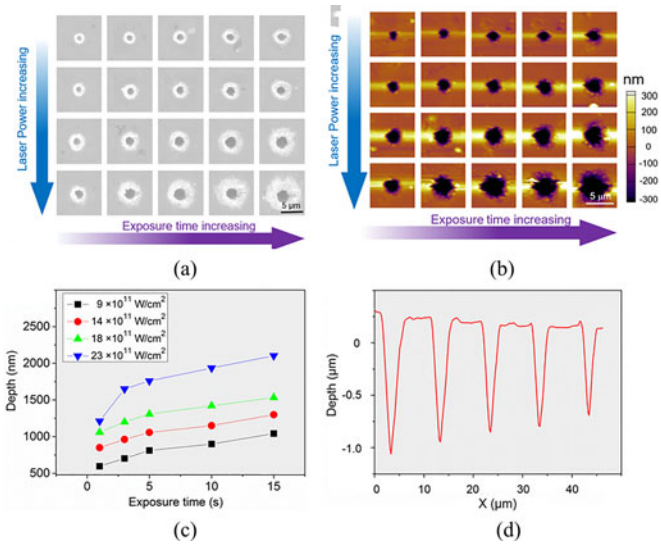

Fig. 3. SEM and AFM images of dots. (a) SEM images of dots for exposure time ranging from 1 s to 15 s and laser power ranging from 9×10^{11} W/cm^2 to 2.3×10^{12} W/cm^2. (b) AFM images of dots for exposure time ranging from 1 s to 15 s and laser power ranging from 9×10^{11} W/cm^2 to 2.3×10^{12} W/cm^2. (c) Relationship between exposure time and depth of dots. With the increasing of exposure time or laser peak intensity, the dot depth obviously becomes deeper. The maximum depth of dot is 2100 nm, and the minimum is 590 nm. (d) Sectional drawing of point depth, the laser peak intensity kept constant (1.4×10^{12} W/cm^2), and the exposure time ranged from 1 s to 15 s with the dot depth becomes deeper from 851 nm to 1300 nm. All the cross sections of dots are V-shaped.

2.3×10^{12} W/cm^2, dot diameter also increases with the prolongation of exposure time, however, the uniformity of processed dots deteriorates obviously. Fig. 2(b) shows the quantitative relationship between the dot diameter and processing parameters. The depth is from 597 nm to 2102 nm according to the atomic force microscope (AFM, MFP-3-D, Asylum Research) measurement [see Fig. 3(b)]. Obviously, with the increase of exposure time or laser peak intensity, the depth becomes deeper [see Fig. 3(c) and (d)] and the cross sections of dots are V-shaped.

The optical microscopy images in Fig. 2(c) reveal the effect of scanning speed ranging from 30 μm/s to 200 μm/s and laser peak intensity ranging from 9×10^{11} W/cm^2 to 2.3×10^{12} W/cm^2 on the line width of ablated grooves by femtosecond laser. When the laser peak intensity is 9×10^{11} W/cm^2, the line width decrease from 1.5 μm to 0.7 μm with the increase of scanning speed from 30 μm/s to 200 μm/s. A minimum line width of 700 nm is achieved. When the laser peak intensity is increased to 1.4×10^{12} W/cm^2, the line width decreases from 2.1 μm to 1.4 μm as scanning speed increase and the uniformity of lines is improved, but when the laser peak intensity is furtherly increased to 2.3×10^{12} W/cm^2, which is beyond the damage threshold, the quality of grooves deteriorates obviously, and the edge of the grooves become coarse and the grooves are ablated deeper. The quantitative dependence between the line width and the parameters were obtained, as shown in Fig. 2(d). These systemic investigation indicates that it is essential to fabricate the crystal devices using proper laser parameters to avoid harmful cracks.

4. A Variety of Designable Microstructures From Nanoparticles, Microline to 2-D Micropatterns

The experiment mentioned above provides us proper parameters for laser processing, then we realized two-dimensional patterning on the surface of perovskite. Fig. 4(a) is the SEM image of grid structure by 1.4×10^{12} W/cm^2 laser peak intensity and 100 μm/s scanning speed. The grid has a period of 20 μm and $\sim$1.5 μm line width. The detailed morphological feature of the grooves

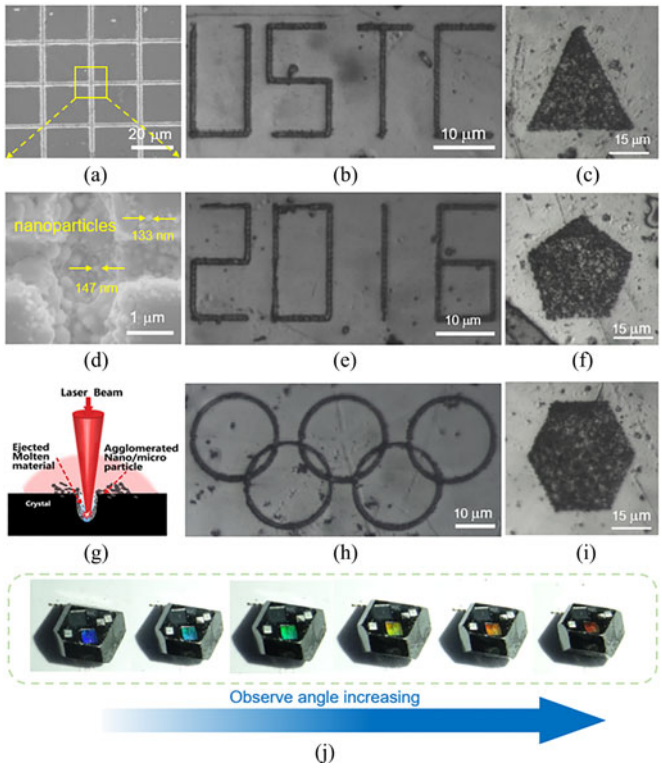

Fig. 4. Variety of designable microstructures from nanoparticles, microline to 2-D micropatterns. (a) Top-view SEM image of grid microstructure. (b) Enlarged image of the 1.5 μm wide microgrid. There are many random nanoparticles in the interior part of the groove with size from 100 to 250 nm. (c) Schematic illustration of laser ablation process. (d)–(f) Optical microscopy images for word "USTC," number "2016," and "Olympic rings," respectively. (g)–(i) Optical microscopy images for 2-D patterns "triangle," "pentagon," and "hexagon," respectively. (j) Digital camera images of structural colors which ranging from dark blue to red. The colors of dark blue, blue, green, yellow, orange and red are observed in 28°, 30°, 33°, 36°, 39° and 41°, respectively.

on the surface of the perovskite structure is shown in Fig. 4(b) Random nanoparticles with size of 100–250 nm are found in the interior part of the groove. During the $CH_3NH_3PbI_3$ crystal ablating process, there is no obvious melting phenomenon and thermal influence on the area surrounding the processed area due to the high laser peak intensity and cold machining effect of ultrafast fs laser [see Fig. 4(c)]. However, in recent reports for continuous wave laser-induced microstructure on perovskite material [26], there is an obvious heat affected zone on the laser-ablating areas. A great amount of nano-pillar like structures are distributed along both edges of the ablated areas due to deposition of nano debris caused by thermal influence which would be reduced to a minimum in femtosecond laser-ablating. This characteristic has been explained by rapid energy deposition in the material. It takes a few hundreds of fs for the electron distribution to reach thermal equilibrium after femtosecond laser ablating [27], [28]. However, the energy transfer time from the electron subsystem to the lattice, which induces thermalization, is of the order of 1–100 ps, depending on the electron–phonon coupling strength of the material. This time is much longer than the time for the electrons to reach thermal equilibrium [29], [30]. Thus, the femtosecond laser can efficiently cause electron heating and generate a hot electron gas that is far from equilibrium with the lattice. Consequently, only a very small fraction of the laser pulse energy is transformed to heat, so that non-thermal processing can be realized [31]. When the pulse width of the laser is shorter than the electron-phonon coupling time in laser-mater interactions, thermal diffusion in the vicinity of the laser ablated area can be almost eliminated. Therefore, one of the most important features of

femtosecond laser processing is that the formation of a heat affected zone is suppressed due to the extremely short pulse with widths of several tens to several hundreds of fs [32]. In addition, various complex micropatterns, such as word "USTC," number "2016," and "Olympic rings," were fabricated by the optimized processing parameters, as shown in Fig. 4(d)–(f). The width of each lines is about 1 μm by 1.4 $\times$ 10^{12} W/cm^2 laser peak intensity and 200 μm/s scanning speed. The overall microstructures are uniform when we exclude the impact of the uneven surface of perovskite itself. Besides linear structures, surface structures, such as triangles, pentagons and hexagons, are also fabricated as shown in Fig. 4(g)–(i). The structures are uniform and some black spots on the Fig. 4 are the perovskite material itself. These results show that femtosecond laser ablating is a powerful microfabrication technology to realize a variety of designable two-dimensional micropatterns on the surface of perovskite material.

To further reduce the heat affected effect and carry out large-area (>2 mm) processing, a regenerative amplified Ti:sapphire fs laser system with low repetition rate (1 kHz) is employed for fabricating 5 μm-period grating. Before laser irradiation, the polarization direction of the laser pulse was adjusted by a linear Glan-Taylor polarizer. The scanning was realized by using a computer controlled high precision X-Y Galvo mirror. To induce large-area micro/nanostructures, the pulse energy of the incident laser is set at 0.1 mJ and the scanning speed is constant (1 mm/s).The step sizes between the adjacent scanning lines is 10 μm. All the experiments are carried out under ordinary room temperature conditions in air too. Due to the grating diffraction effect, the perovskite surface is colorful which means various structural colors ranging from dark blue to red can be observed in different viewing angles. In order to systematically investigate the influence of the observe angle on the formation of structural colors, a color measuring system is configured. For example, dark blue, blue, green, yellow, orange and red are observed in 28°, 30°, 33°, 36°, 39° and 41°, respectively [see Fig. 4(j)].

5. Characterizing the Fluorescence Processing of This Material After Laser Ablating

X-ray diffraction (XRD) is a powerful tool to characterize the quality of crystalline materials. Before laser processing on the perovskite material, we use it to detect the structural information of the sample to determine the sample which we growth were perovskite single crystal. The measurement was taken by using a focused X-ray, with Cu Kα1 line (λ = 1.5418 Å) with V = 40 KV and I = 40 mA. The powder X-ray diffraction (PXRD; Fig. 5(a)) pattern shows a set of strong diffraction peaks that can be assigned to a pure tetragonal $CH_3NH_3PbI_3$ crystal structure (space group I4cm, a = b = 8.896 Å, c = 12.637 Å), in good agreement with the calculated XRD patterns from the single crystal model. The habit of all single crystals of $CH_3NH_3PbI_3$ exhibits several large planes, and we choose a proper one which is identified to be the (112) for laser processing surface.

For comparison, processed area and unprocessed area of the samples were measured. Before laser processing, the natural facet (112) is subjected to XRD measurement, and the diffraction data is shown by the black line in Fig. 5(b). Then laser processing is performed in the measured region. The processing area is subjected to XRD measurement immediately, with the diffraction data shown by the red line in Fig. 5(b). The measurement was taken by a parallel X-ray, with Cu Kα line (λ = 1.5406 Å) with V = 40 KV and I = 30 mA. The processed area is 1.5 mm $\times$ 1 mm, and the fabrication parameters are 100 μm/s scanning speed and 1.4 $\times$ 10^{12} W/cm^2 laser peak intensity. It can be easily found that the position of diffraction peak doesn't change obviously while the relative strength between diffraction peaks has a significant change after processing. The change is probably caused by the micro/nano structures formed on the surface of crystal, which improves the surface roughness of the crystal.

To understand the laser processing effect on the optical property of perovskite crystal, the fluorescence were measured. Fig. 5(c) and (d) shows the results of two comparative experiments. Firstly, the scanning speed kept constant (100 μm/s), and the laser peak intensity ranged from 9 $\times$ 10^{11} W/cm^2 to 2.3 $\times$ 10^{12} W/cm^2. From the measured fluorescence as shown in Fig. 5(c), it

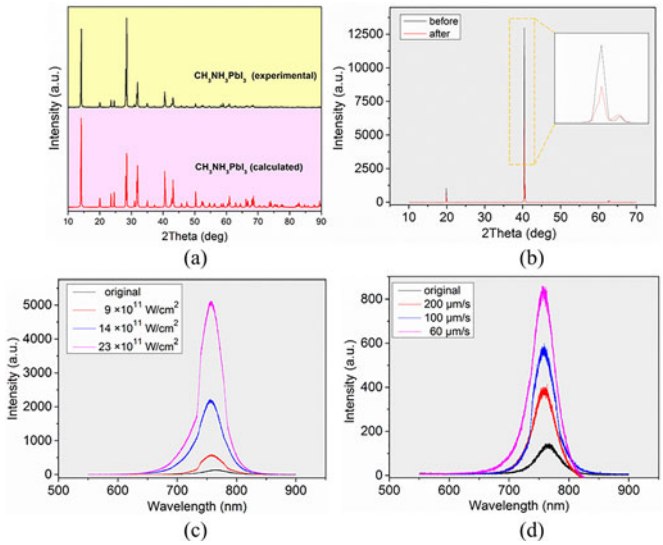

Fig. 5. Calculated and experimental powder X-ray diffraction patterns for $CH_3NH_3PbI_3$ and characterization of fluorescence properties. (a) Calculated and experimental powder X-ray diffraction patterns for $CH_3NH_3PbI_3$, experimental PXRD confirming the tetragonal phase of the single structure. (b) X-ray diffraction pattern before and after processing on the (112) plane. (c) Fluorescence when scanning speed is constant and laser peak intensity varies from 9×10^{11} W/cm^2 to 1.8×10^{12} W/cm^2. (d) Fluorescence figure when laser peak intensity is constant and scanning speed changes from 60 μm/s to 200 μm/s. Both (c) and (d) show that the fluorescence peak strength of processed area appears to have an obvious growing trend with the increase of laser peak intensity or decrease of scanning speed.

can be seen that, compared with the unprocessed area of which the PL spectrum at room temperature is centered at 770 nm, the fluorescence peak strength of processed area appears to have an obvious growing trend with the increase of laser peak intensity, and the PL peak has a blue-shifted ($<$2 nm) but still around 770 nm. Second, the laser peak intensity kept constant (9×10^{11} W/cm^2), and the scanning speed ranged from 60 μm/s to 100 μm/s. Similarly, compared with unprocessed area, the fluorescence peak strength of processed area appears to have an obvious growing trend with the decrease of scanning speed, and the PL peak has a blue-shifted ($<$2 nm) but also around 770 nm [see Fig. 5(d)]. The little change in PL peak position indicates that the area processed using femtosecond laser still consists of all elements of $CH_3NH_3PbI_3$ crystal material system.

In order to investigate the reason of fluorescence peak strength change, scanning electron microscope (SEM) is adopted to observe laser-induced surface topography change. Presented in Fig. 6(a) is the SEM image of unprocessed area, which has a smooth surface. Fig. 6(b) and (c) shows the results after laser ablating with 1.4×10^{12} W/cm^2 laser peak intensity and 200 μm/s scanning speed, where the characteristic features are nanogroove and random nanoparticles with size down to hundreds of nanometers. Furtherly, atomic force microscope is adopted to quantitatively analyze the variation of surface roughness in an area of 10 μm $\times$ 10 μm. Fig. 6(d) indicates that, the surface roughness Ra (arithmetical mean deviation of the profile) of unprocessed area is 4.101 nm and when the scanning speed keep constant (100 μm/s), the surface roughness increase from 114.332 nm to 245.149 nm with the increase of laser peak intensity from 9×10^{11} W/cm^2 to 1.8×10^{12} W/cm^2. Similarly, when the laser peak intensity kept constant (9×10^{11} W/cm^2), the surface roughness increase from 40.924 nm to 153.791 nm with the decrease of scanning speed from 200 to 50 μm/s [see Fig. 6(e)]. The changes of surface roughness can be observed more intuitively from the AFM images in Fig. 6(d) and (e).

On one hand, the increase of surface roughness means more grain nanostructures on the surface. Those grain nanostructures have large specific surface area due to their small volume. Because of the increasing of atoms on the surface, positron or negatron stimulated by light on the surface have a growing bound effect by the passivated surface. The light power absorbed by surface grows

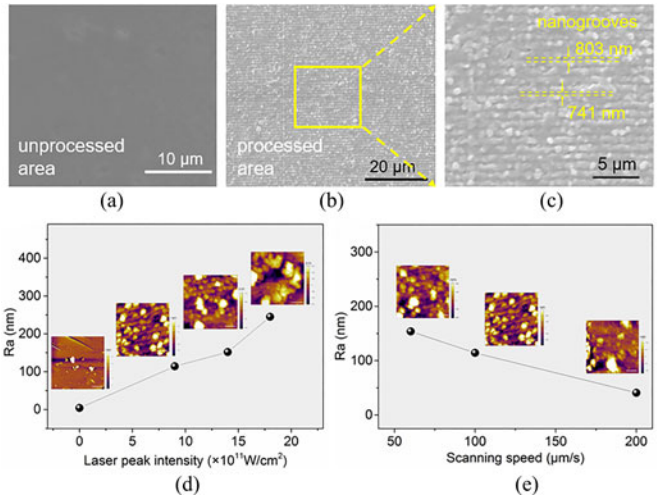

Fig. 6. Increased surface roughness of processed area which is responsible for fluorescence enhancement. (a) SEM image of unprocessed area. (b) SEM image of processed area after laser ablating with 1.4×10^{12} W/cm^2 laser peak intensity and 200 μm/s scanning speed. (c) Enlarged image of the nanogroove. There are many random nanoparticles with size down to about hundreds of nanometers in the interior part of the groove. (d) Relationship between laser peak intensity and surface roughness Ra. The maximum value of surface roughness Ra is 245.149 nm. (e) Relationship between scanning speed and surface roughness Ra. The maximum value of surface roughness Ra is 153.791nm. The AFM images in both (d) and (e) show the increase of surface roughness with the increase of laser peak intensity or decrease of scanning speed.

as well, so that the excitation and the fluorescence intensity of perovskite was enhanced. On the other hand, since the perovskite material have a high refractive index itself, only a small portion of the light, which is radiated by carrier recombination and emitted to the outside, can radiate into free space, most of it is absorbed and dissipated by the material after the repeatedly total reflection by the interface between the material and the air. Manufacturing grain nanostructures in the surface can increase the randomness of the incidence angle, reducing the possibility of the total reflection when the light reaches the interface, which can thereby increasing the strength of the fluorescence peak. At present, perovskite material is a promising material in the fabrication of light emitting diode (LED) and how to improve light extraction efficiency has become a hot research traitor. Improve the photoluminescence intensity by surface rough technology has an obvious advantages in practice. Compared with traditional methods (dry etching and wet etching), surface rough by femtosecond laser ablating have many preponderance such as high controllably, high reproducibility, no change to the crystal material system. Femtosecond laser nanoprocessing of single-crystal perovskite which improve light extraction efficiency of perovskite optoelectronic devices can provide a new idea for this field.

6. Conclusion

In this paper, we have proposed a technique using femtosecond laser microfabrication to produce micro/nanostructures on the $CH_3NH_3PbI_3$ crystal surface for the first time. A variety of micropatterns from nanoparticles, 1-D micropores, microline to 2-D micropatterns have been successfully realized. The quantitative relationship between laser processing parameters and quality of micropatterns was investigated. Moreover, colorful perovskite surfaces were obtained by fabricating periodic grating microstructures. The XRD and photoluminescence measurements reveal that femtosecond laser processing increases the surface roughness of the crystal and improves the fluorescence intensity of perovskite. These studies would benefit better understanding of the optical property of single crystal perovskite and the fabricated perovskite microstructures by femtosecond laser processing may find broader applications in perovskite-based optoelectronic devices.

References

[1] Y. X. Zhao and K. Zhu, "Organic–inorganic hybrid lead halide perovskites for optoelectronic and electronic applications," *Chem. Soc. Rev.*, vol. 45, no. 3, pp. 655–689, 2016.

[2] H. J. Snaith, "Perovskites: The emergence of a new era for low-cost, high-efficiency solar cells," *J. Phys. Chem. Lett.*, vol. 4, no. 21, pp. 3623–3630, 2013.

[3] T. Ye, W. F. Fu, J. K. Wu, Z. K. Yu, H. Z. Chen, and H. Y. Li, "Single-crystalline lead halide Perovskite arrays for solar cells," *J. Mater. Chem. A*, vol. 4, no. 4, pp. 1214–1217, 2016.

[4] J. J. Shi, X. Xu, D. M. Li, and Q. B. Meng, "Interfaces in perovskite solar cells," *Small*, vol. 11, no. 21, pp. 2472–2486, 2015.

[5] S. N. Habisreutinger, T. Leijtens, G. E. Eperon, S. D. Stranks, R. J. Nicholas, and H. J. Snaith, "Carbon nanotube/polymer composites as a highly stable hole collection layer in perovskite solar cells," *Nano Lett.*, vol. 14, no. 10, pp. 5561–5568, 2014.

[6] A. Kojima, K. Teshima, Y. Shirai, and T. Miyasaka, "Organometal halide perovskites as visible-light sensitizers for photovoltaic cells," *J. Amer. Chem. Soc.*, vol. 131, no. 17, pp. 6050–6051, 2009.

[7] Y. Y. Dang, D. X. Ju, L. Wang, and X. T. Tao, "Recent progress in the synthesis of hybrid halide perovskite single crystals," *CrystEngComm*, vol. 18, no. 24, pp. 4476–4484, 2016.

[8] J. Berry *et al.*, "Hybrid organic–inorganic perovskites (HOIPs): Opportunities and challenges," *Adv. Mater.*, vol. 27, no. 35, pp. 5102–5112, 2015.

[9] G. J. A. H. Wetzelaer, M. Scheeper, A. M. Sempere, C. Momblona, J. Avila, and H. J. Bolink, "Trap-assisted non-radiative recombination in organic–inorganic perovskite solar cells," *Adv. Mater.*, vol. 27, no. 11, pp. 1837–1841, 2015.

[10] A. Y. Mei *et al.*, "A hole-conductor–free, fully printable mesoscopic Perovskite solar cell with high stability," *Science*, vol. 345, no. 6194, pp. 295–298, 2014.

[11] Y. C. Shao, Z. G. Xiao, C. Bi, Y. B. Yuan, and J. S. Huang, "Origin and elimination of photocurrent hysteresis by fullerene passivation in $CH_3NH_3PbI_3$ planar heterojunction solar cells," *Nature Commun.*, vol. 5, 2014, Art. no. 5784.

[12] Y. C. Liu *et al.*, "Two-inch-sized perovskite $CH_3NH_3PbX_3$ (X= Cl, Br, I) crystals: Growth and characterization," *Adv. Mater.*, vol. 27, no. 35, pp. 5176–5189, 2015.

[13] D. Shi *et al.*, "Low trap-state density and long carrier diffusion in organolead trihalide perovskite single crystals," *Science*, vol. 347, no. 6221, pp. 519–522, 2015.

[14] G. Maculan *et al.*, "$CH_3NH_3PbCl_3$ single crystals: Inverse temperature crystallization and visible-blind UV-photodetector," *J. Phys. Chem. Lett.*, vol. 6, no. 19, pp. 3781–3789, 2015.

[15] M. I. Saidaminov *et al.*, "Planar-integrated single-crystalline perovskite photodetectors," *Nature Commun.*, vol. 6, 2015, Art. no. 8724.

[16] S. S. Chou *et al.*, "Laser direct write synthesis of lead halide perovskites," *J. Phys. Chem. Lett.*, vol. 7, no. 19, pp. 3736–3741, 2016.

[17] Y. L. Hu *et al.*, "Laser printing hierarchical structures with the aid of controlled capillary-driven self-assembly," *Proc. Nat. Acad. Sci. USA*, vol. 112, no. 22, pp. 6876–6881, 2015.

[18] A. D. Wang *et al.*, "Mask-free patterning of high-conductivity metal nanowires in open air by spatially modulated femtosecond laser pulses," *Adv. Mater.*, vol. 27, no. 40, pp. 6238–6243, 2015.

[19] D. Wu, J. Xu, L. G. Niu, S. Z. Wu, K. Midorikawa, and K. Sugioka, "In-channel integration of designable microoptical devices using flat scaffold-supported femtosecond-laser microfabrication for coupling-free optofluidic cell counting," *Light Sci. Appl.*, vol. 4, no. 1, p. e228, 2015.

[20] Z. F. Deng *et al.*, "Dragonfly-eye-inspired artificial compound eyes with sophisticated imaging," *Adv. Funct. Mater.*, vol. 26, no. 12, pp. 1995–2001, 2016.

[21] Y. L. Sun *et al.*, "Aqueous multiphoton lithography with multifunctional silk-centred bio-resists," *Nature Commun.*, vol. 6, 2015, Art. no. 8612.

[22] B. Zheng *et al.*, "Femtosecond laser fabrication of cavity microball lens (CMBL) inside a PMMA substrate for super-wide angle imaging," *Small*, vol. 11, no. 25, pp. 3007–3016, 2015.

[23] F. Chen and J. R. V. D. Aldana, "Optical waveguides in crystalline dielectric materials produced by femtosecond-laser micromachining," *Laser Photon. Rev.*, vol. 8, no. 2, pp. 251–275, 2014.

[24] Y. Y. Dang *et al.*, "Bulk crystal growth of hybrid perovskite material $CH_3NH_3PbI_3$," *CrystEngComm.*, vol. 17, no. 3, pp. 665–670, 2015.

[25] H. S. Kim, S. H. Im, and H. G. Park, "Organolead halide perovskite: New horizons in solar cell research," *J. Phys. Chem. C*, vol. 118, no. 11, pp. 5615–5625, 2014.

[26] P. K. Kanaujia and G. V. Prakash, "Laser-induced microstructuring of two-dimensional layered inorganic–organic perovskites," *Phys. Chem. Chem. Phys.*, vol. 18, no. 14, pp. 9666–9672, 2016.

[27] W. S. Fann, R. Storz, H. W. Tom, and J. Bokor, "Electron thermalization in gold," *Phys. Rev. B*, vol. 46, no. 20, pp. 13592–13595, 1992.

[28] C. K. Sun, F. Vallee, L. H. Acioli, E. P. Ippen, and J. G. Fujimoto, "Femtosecond-tunable measurement of electron thermalization in gold," *Phys. Rev. B*, vol. 50, no. 20, pp. 15337–15348, 1994.

[29] J. Hohlfeld, S. S. Wellershoff, J. Gudde, U. Conrad, V. Jahnke, and E. Matthias, "Electron and lattice dynamics following optical excitation of metals," *Chem. Phys.*, vol. 251, no. 1, pp. 237–258, 2000.

[30] S. S. Wellershoff, J. Hohlfeld, J. Gudde, and E. Matthias, "The role of electron–phonon coupling in femtosecond laser damage of metals," *Appl. Phys. A*, vol. 69, no. 1, pp. S99–S107, 1999.

[31] R. R. Gattass and E. Mazur, "Femtosecond laser micromachining in transparent materials," *Nature Photon.*, vol. 2, no. 4, pp. 219–225, 2008.

[32] K. Sugioka and Y. Cheng, "Femtosecond laser three-dimensional micro-and nanofabrication," *Appl. Phys. Rev.*, vol. 1, no. 4, 2014, Art. no. 041303.